



# Tri-metallic AuPdIr nanoalloy towards efficient hydrogen generation from formic acid

Dong-Xue Liu<sup>1</sup>, Yi-Tong Zhou<sup>1</sup>, Yong-Fu Zhu, Ze-Yu Chen, Jun-Min Yan<sup>\*</sup>, Qing Jiang

Key Laboratory of Automobile Materials, Ministry of Education, School of Materials Science and Engineering, Jilin University, Changchun 130022, China

## ARTICLE INFO

### Keywords:

Formic acid  
Dehydrogenation  
Heterogeneous catalyst  
High activity  
DFT calculation

## ABSTRACT

Formic acid (FA), as a safe and renewable hydrogen storage material, attracts extensive attention. Herein, an efficient catalyst Au<sub>0.35</sub>Pd<sub>0.5</sub>Ir<sub>0.15</sub> nanoalloy supported on NH<sub>2</sub>-N-rGO has been successfully synthesized and applied for hydrogen generation from FA. It is found by density function theory (DFT) calculation that addition of Ir into AuPd alloy can change the initial adsorption configuration of HCOOH\* and thus reduce the energy barrier of rate determining step (RDS) of FA dehydrogenation. As a result, Au<sub>0.35</sub>Pd<sub>0.5</sub>Ir<sub>0.15</sub>/NH<sub>2</sub>-N-rGO displays 100% conversion, 100% selectivity even after 150 days for FA dehydrogenation at 298 K, and the initial turnover frequency (TOF) can reach the recorded value (12781.2 h<sup>-1</sup>) without any additives. More interestingly, it is proved to be a universal method to design the effective catalysts for hydrogen generation from FA by the high activities of other tri-metallic alloys with addition of other high  $\gamma$  elements (such as Pt, Rh, and Ru).

## 1. Introduction

Hydrogen (H<sub>2</sub>), due to its abundant, clean, environment-friendly and renewable properties, is regarded as the most promising energy carrier to mitigate global warming and alleviate the depletion of petroleum resources [1–4]. And the main problem for widespread use of H<sub>2</sub> is unsafe and inefficient storage. Formic acid (HCOOH, FA) has attracted lots of attention, owing to its high hydrogen content (4.4 wt%), non-toxicity, low-flammability, high stability, and easy accessibility [5–9]. Generally, FA decomposition occurs in two ways: dehydrogenation and dehydration [10], while the latter path, for the purpose of H<sub>2</sub> generation, should be avoided. A lot of homogeneous and heterogeneous catalysts are found to be effective on FA dehydrogenation. Although homogeneous catalysts, especially some Ir complexes, demonstrate good catalytic activities [11–18], problems in separating and recovering still remain as a big challenge. In addition, most homogeneous systems require elevated temperature or extra additives to reach relatively high catalytic activities [5]. Therefore, the development of efficient and robust heterogeneous catalysts becomes very important.

As reported, palladium (Pd) [19–25] and Pd based bimetallic nanoparticles (NPs) [26–34], especially AuPd alloy, are highly active for FA dehydrogenation at low temperature. A large number of data show that AuPd alloy has a significant advantage in bimetallic catalysts, while

some of them need sodium formate (SF) additive [30–34]. The DFT calculation reveals that the dehydrogenation of FA includes four steps: (I) bond cleavage of O-H (denoted as TS1), (II) rearrangement of bi-HCOO\* (TS2), (III) bond cleavage of C-H (TS3), and (IV) H<sub>2</sub> desorption (TS4). Pure Pd can facilitate the O-H bond cleavage but discourage the rearrangement of bi-HCOO\*, (where “\*” represents adsorbed state) and H<sub>2</sub> desorption [35]. Therefore, alloying with a low surface energy ( $\gamma$ ) element, such as Au (1.52 J/m<sup>2</sup>) [36], to weaken the adsorption capability of the AuPd alloy catalyst, is a good way to regulate the RDS and energy barrier ( $E_{\text{bar}}$ ) [35]. Notably, the best metal ratio of Au: Pd is 1:1, because excessive Au leads to difficulty in breaking the O-H bond. In this sense, adding a small amount of the high  $\gamma$  element to replace a part of Au may change the initial adsorption configuration of HCOOH\* and further reduce the energy barrier.

Normally, an efficient heterogeneous catalyst should have small particle size and good dispersion in reaction solution to provide more active sites. In our previous work, we found that N-doped and NH<sub>2</sub>-functionalized reduced graphene oxide (NH<sub>2</sub>-N-rGO) is a good substrate to guarantee the nanoparticles with ultrafine sizes and good dispersion on it [28,35]. RGO has large surface area and excellent stability [37]; doped N atoms and hydrophilic NH<sub>2</sub>- species can anchor metal anions and further help to form small particles, and increase the hydrophilicity of catalyst to fully contact with the reactants in aqueous solution [35,38,

\* Corresponding author.

E-mail address: [junminyan@jlu.edu.cn](mailto:junminyan@jlu.edu.cn) (J.-M. Yan).

<sup>1</sup> These authors have contributed equally.

39].

Herein, Ir is chosen as an element with high  $\gamma$  ( $3.19 \text{ J/m}^2$ ) to form  $\text{Au}_{0.35}\text{Pd}_{0.5}\text{Ir}_{0.15}/\text{NH}_2\text{-N-rGO}$  [36]. As expected, the supported  $\text{Au}_{0.35}\text{Pd}_{0.5}\text{Ir}_{0.15}$  displays 100% selectivity of dehydrogenation and 100% conversion at room temperature. The initial TOF of  $12781.2 \text{ h}^{-1}$  is almost three times of supported  $\text{Au}_{0.5}\text{Pd}_{0.5}$ . As far as we know, this value of TOF is never reached by other heterogeneous catalysts, and is also comparable to most of the homogenous catalysts even at high temperatures. Based on the DFT calculations, tri-metallic nanoalloys with a high  $\gamma$  element of Ir to partially replace Au can obviously facilitate the rearrangement of bi-HCOO\* (TS2) without inhibiting O-H bond cleavage (TS1), and thus the activity of the catalyst is significantly improved, which has also been proved by the good performances of other supported tri-metallic nanoalloys of AuPdPt, AuPdRh, and AuPdRu.

## 2. Experimental section

### 2.1. Materials

Graphite flake (C, Alfa Aesar, 325 mesh, 99.8%), hydrogen peroxide ( $\text{H}_2\text{O}_2$ , Beijing Chemical Works, 30%), potassium permanganate ( $\text{KMnO}_4$ , Sinopharm Chemical Reagent Co., Ltd, > 99.99%), sulfuric acid ( $\text{H}_2\text{SO}_4$ , Beijing Chemical Works, 98%), phosphoric acid ( $\text{H}_3\text{PO}_4$ , Sinopharm Chemical Reagent Co., Ltd, 85%), hydrochloric acid (HCl, Beijing Chemical Works, 36–37%) were chosen to synthesize GO. Formic acid (FA,  $\text{HCOOH}$ , Sigma-Aldrich, 96%) was chosen as reactant. Sodium chloride (NaCl, Sinopharm Chemical Reagent Co., Ltd, > 99.5%), iridium chloride ( $\text{IrCl}_3$ , Aladdin Chemistry Co., Ltd, 99.8% metals basis), potassium chloroplatinate (II) ( $\text{K}_2\text{PtCl}_4$ , Sinopharm Chemical Reagent Co., Ltd, Pt > 45%), palladium (II) chloride ( $\text{PdCl}_2$ , Sinopharm Chemical Reagent Co., Ltd, Pd > 59%), rhodium chloride hydrate ( $\text{RhCl}_3 \cdot 3\text{H}_2\text{O}$ , Aladdin Chemistry Co., Ltd, Rh 38.5–42.5%), ruthenium chloride anhydrous ( $\text{RuCl}_3$ , Aladdin Chemistry Co., Ltd, Ru 45–55%), and tetrachloroauric (III) acid tetrahydrate ( $\text{HAuCl}_4 \cdot 4\text{H}_2\text{O}$ , Sinopharm Chemical Reagent Co., Ltd, Au > 47.8%) were chosen as the precursor. 3-Aminopropyl triethoxysilane (APTS,  $\text{C}_9\text{H}_{23}\text{NO}_3\text{Si}$ , Aladdin Chemistry Co., Ltd, 99%) was chosen as dispersing agent and the source of nitrogen and amino groups. The sodium borohydride ( $\text{NaBH}_4$ , Aladdin Reagent Co., Ltd) was the reductant. Sodium hydroxide (NaOH, Sinopharm Chemical Reagent Co., Ltd, 96.0%), and ammonia solution ( $\text{NH}_4\text{OH}$ , Sinopharm Chemical Reagent Co., Ltd, 25–28%) were used to synthesize N-GO. Boron nitride (BN, Aladdin Chemistry Co., Ltd, 99.9%), and titanium (IV) oxide ( $\text{TiO}_2$ , Sinopharm Chemical Reagent Co., Ltd,  $\geq 98\%$ ) were selected as substrate materials for comparison.

By reverse osmosis, ion exchange and filtering, we can obtain the deionized water ( $18.2 \text{ M}\Omega \cdot \text{cm}$ ).

### 2.2. Synthesis of catalysts

#### 2.2.1. Synthesis of graphene oxide (GO)

The way to synthesize GO is a kind of modified Hummers' method [40]. Firstly, 3.002 g graphite powder was mixed with 18.005 g  $\text{KMnO}_4$  and added into the  $\text{H}_2\text{SO}_4/\text{H}_3\text{PO}_4$  (9:1, 400 mL) solution little by little. The above suspension was stirred for 4 h, and then heated to about 323 K for 14 h. Thereafter, some ice was added carefully until the suspension was cooled to 298–308 K.  $\text{H}_2\text{O}_2$  (16 mL, 30%) and deionized water were poured to keep the volume of the liquid around 1600 mL. The suspension was stirred for 8 h, and then centrifuged (10,000 r/min for 7 min). After that, 500 mL of water was poured into the solid material, and after stirring for 1 h, 200 mL HCl (36–37%) was added and stirred for another 15–20 h. Finally, the suspension was centrifuged 10–15 times (10,000 r/min) with deionized water until the liquid is neutral.

#### 2.2.2. Synthesis of N-GO

First, NaOH (100.0 mg) and  $\text{NH}_4\text{OH}$  (8 mL) were dissolved into the as prepared GO solution (1.5 mg/mL, 30 mL) under stirring. And then,

the mixed solution was poured into a Teflon-lined autoclave for reaction at 453 K for 3 h to get N-GO. The product was centrifuged (12,000 r/min for 10 min) and washed for 4 times by deionized water for later use.

#### 2.2.3. Synthesis of $\text{Au}_{0.35}\text{Pd}_{0.5}\text{Ir}_{0.15}/\text{NH}_2\text{-N-rGO}$

Firstly,  $\text{Na}_2\text{PdCl}_4$  aqueous solution (0.02 M) was firstly prepared by dissolving NaCl (1.0 mmol) and  $\text{PdCl}_2$  (0.5 mmol) into 25 mL  $\text{H}_2\text{O}$  with magnetic stirring for 3 h until the solution became clear and transparent. Thereafter, GO aqueous solution (1.5 mg/mL, 20 mL) and 0.4 mL of APTS were mixed and sonicated for 20 min. And then, 0.02 M aqueous solutions of  $\text{HAuCl}_4 \cdot 4\text{H}_2\text{O}$  (1.75 mL),  $\text{Na}_2\text{PdCl}_4$  (2.5 mL), and  $\text{IrCl}_3$  (0.75 mL) were added to above APTS/GO solution, stirring for 5 min. After that, 30.0 mg of  $\text{NaBH}_4$  was added with stirring for 30 min. Finally, the obtained solid was centrifuged and washed 4 times by deionized water (10,000 r/min for 4 min) to get  $\text{Au}_{0.35}\text{Pd}_{0.5}\text{Ir}_{0.15}/\text{NH}_2\text{-N-rGO}$ .

Other tri-/bi-/mono-metallic NPs supported on  $\text{NH}_2\text{-N-rGO}$  were synthesized with the similar method mentioned above. And  $\text{Au}_{0.35}\text{Pd}_{0.5}\text{Ir}_{0.15}$  supported on different substrates, including rGO, N-rGO, BN, and  $\text{TiO}_2$ , as well as  $\text{Au}_{0.35}\text{Pd}_{0.5}\text{Ir}_{0.15}$  with only APTS were also prepared through the similar method.

### 2.3. FA dehydrogenation experiments

The as-prepared catalyst was kept in a two-necked flask and dispersed in 10 mL of deionized water. One neck was connected with a funnel for pressure-equalization, which contained FA (1 M, 5 mL for each time), the other one was connected with the gas buret (Fig. S1). The flask was kept in a water bath (298 K) under stirring. The released gas was measured by a water-filled graduated glass tube, which was connected with the reactor ( $V_{\text{absolute}} = V_{\text{observation}} - V_{\text{blank}}$ ). All of the experiments have been repeated at least 3 times, and the experiments could be repeated successfully.

### 2.4. Materials characterization

Fourier transform infrared (FTIR) spectra were measured at 298 K on a NEXUS-670 spectrometer. Transmission electron microscope (TEM, JEM-2100F) was applied for the morphology analysis, and the sample supporter was amorphous carbon coated copper grids. STEM was performed on a Grand ARM resolution electron microscope (JEM-ARM-300F). Rigaku D/Max-2550 with Cu K $\alpha$  and MiniFlex-600 was chosen to perform the Powder X-ray diffraction (XRD). Ultima Expert (LT) instrument was applied for the Inductively coupled plasma optical emission spectrometry (ICP-OES). Gas composition was detected by mass spectrometry (MS, Hiden HPR40, the carrying gas was Ar). Gas chromatograph (GC-7900) with thermal conductivity detector (TCD) was used to distinguish  $\text{N}_2$  and CO, and gas chromatograph (Thermo-scientific Trace 1300) equipped with pulse discharge detector (PDD) was further applied to detect CO. X-ray photoelectron spectrometer (XPS) spectra were carried out on an ESCALAB-250Xi with the mono-chromatized Al K $\alpha$  as excitation source.

## 3. Results and discussion

### 3.1. Characterization of AuPdIr catalyst

To improve the efficiency of dehydrogenation from FA,  $\text{Au}_{0.35}\text{Pd}_{0.5}\text{Ir}_{0.15}$  supported on  $\text{NH}_2\text{-N-rGO}$  is prepared and characterized. The formation of  $\text{NH}_2\text{-N-rGO}$  substrate is proved by the fourier transform infrared (FTIR) spectrum in Fig. S2. As seen in Fig. 1A–C, the typical transmission electron microscope (TEM) images demonstrate that the  $\text{Au}_{0.35}\text{Pd}_{0.5}\text{Ir}_{0.15}$  NPs with an average size of 2.6 nm are well dispersed on  $\text{NH}_2\text{-N-rGO}$  substrate. However, pure  $\text{Au}_{0.35}\text{Pd}_{0.5}\text{Ir}_{0.15}$  with (3.9 nm) or without APTS (9.3 nm), as well as  $\text{Au}_{0.35}\text{Pd}_{0.5}\text{Ir}_{0.15}$  supported on rGO (3.6 nm), N-rGO (4.0 nm), BN (3.0 nm), and  $\text{TiO}_2$  (4.7 nm) have bigger sizes and more or less aggregations (Fig. S3). The image of high

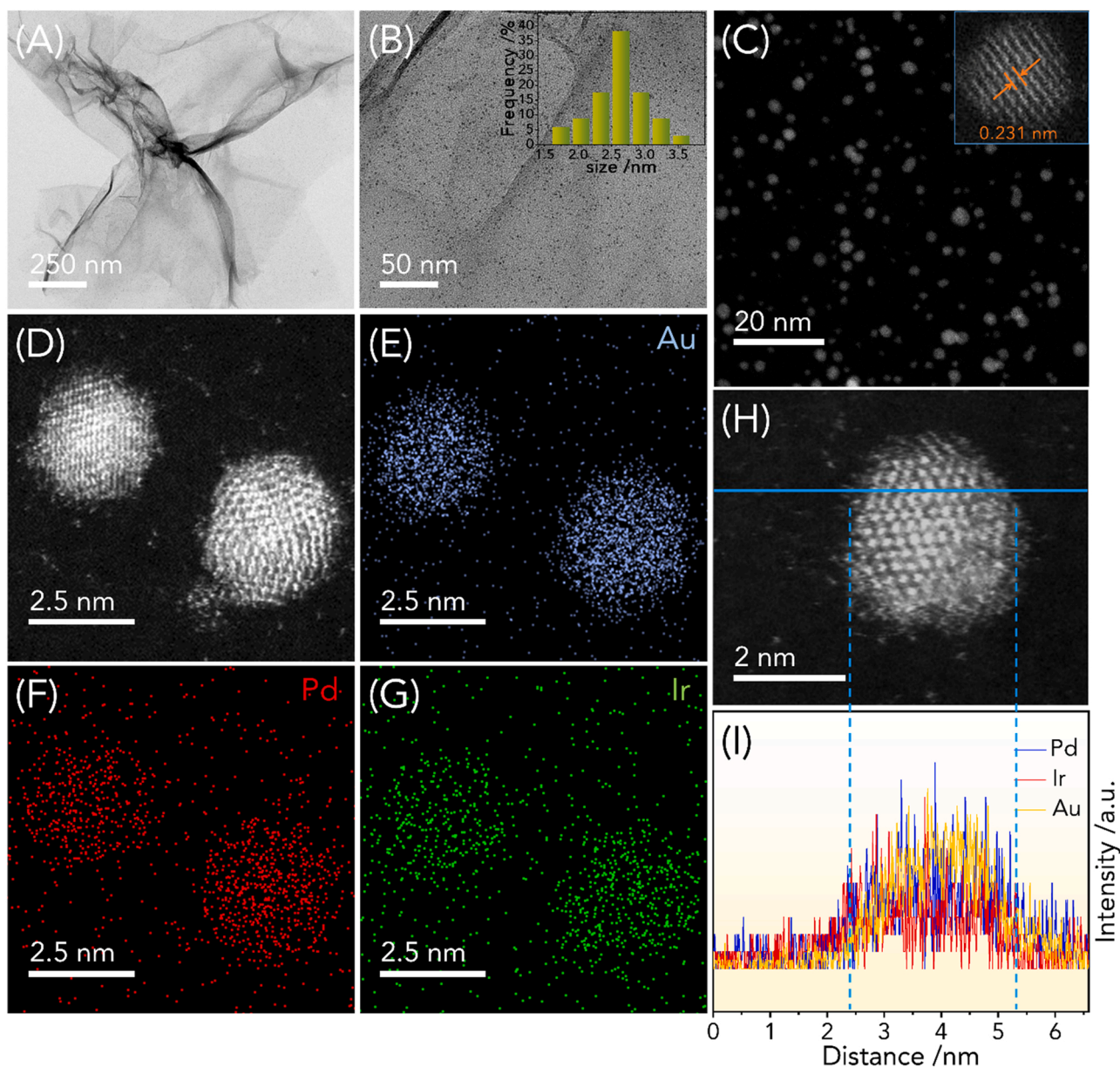


**Fig. 1.** TEM images of  $\text{Au}_{0.35}\text{Pd}_{0.5}\text{Ir}_{0.15}/\text{NH}_2\text{-N-rGO}$  with (A) low and (B) middle resolutions, inset is the corresponding size distribution. (C) HAADF image of  $\text{Au}_{0.35}\text{Pd}_{0.5}\text{Ir}_{0.15}/\text{NH}_2\text{-N-rGO}$ , inset is the corresponding high resolution TEM image. (D) HAADF-STEM image of  $\text{Au}_{0.35}\text{Pd}_{0.5}\text{Ir}_{0.15}/\text{NH}_2\text{-N-rGO}$  and (E-G) the corresponding mappings of Au, Pd, and Ir. (H) HAADF-STEM image and (I) the corresponding EDS line scans of  $\text{Au}_{0.35}\text{Pd}_{0.5}\text{Ir}_{0.15}/\text{NH}_2\text{-N-rGO}$ .

resolution TEM (HRTEM, Fig. 1C, inset) shows the lattice spacing of 0.231 nm, which is among the (111) planes of face-centered cubic (fcc) Ir (0.221 nm, JCPDS: 65–1686) [41], Pd (0.224 nm, JCPDS: 65–2867), and Au (0.235 nm, JCPDS: 65–2870) [35]. The spherical aberration-corrected high-angle annular dark-field scanning transmission electron microscopy (HAADF-STEM) image, energy dispersive X-ray spectroscopy (EDS) elemental mappings (Fig. 1D-G) and line scans (Fig. 1H-I) for Au, Pd, and Ir in the supported  $\text{Au}_{0.35}\text{Pd}_{0.5}\text{Ir}_{0.15}$  composite prove the uniform existences of Au, Pd, and Ir in one nanoparticle.

In addition, The X-ray diffraction (XRD) pattern of  $\text{Au}_{0.35}\text{Pd}_{0.5}\text{Ir}_{0.15}/\text{NH}_2\text{-N-rGO}$  (Fig. 2A) shows a characteristic peak at around  $39^\circ$  among those for fcc phases of Au, Pd, and Ir, which may be due to the alloy structure of  $\text{Au}_{0.35}\text{Pd}_{0.5}\text{Ir}_{0.15}$ . Owing to the highly dispersed and ultra-small-sized particles, the peak is broad with low intensity [42]. To observe its alloy structure more clearly, the specimen is heat-treated in Ar atmosphere at 773 K for 3 h (Fig. S4). As a result,  $\text{Au}_{0.35}\text{Pd}_{0.5}\text{Ir}_{0.15}$  still shows the same characteristic peaks for an fcc phase but only with

the increased intensities, demonstrating that the three metallic elements are formed the alloy structure. X-ray photoelectron spectrometry (XPS) spectra in Fig. 2B-D show that binding energies of Au 4f, Pd 3d, and Ir 4f in pure  $\text{Au}_{0.35}\text{Pd}_{0.5}\text{Ir}_{0.15}$  alloy are higher than that in  $\text{Au}_{0.35}\text{Pd}_{0.5}\text{Ir}_{0.15}/\text{NH}_2\text{-N-rGO}$ , indicating the electrons transferring from substrate to AuPdIr alloy. This strong metal-support interaction (SMSI) proves that the AuPdIr nanoalloys are successfully supported on the substrate through the co-reduction method. Moreover, compared with the monometallic Au, Pd, Ir supported on  $\text{NH}_2\text{-N-rGO}$ , the binding energy of metallic Au 4f in  $\text{Au}_{0.35}\text{Pd}_{0.5}\text{Ir}_{0.15}/\text{NH}_2\text{-N-rGO}$  is shifted to the lower value (from 84.0 to 83.6 eV) [35], whereas those for metallic Pd 3d (from 335.6 to 335.7 eV) and Ir 4f (from 61.1 to 61.3 eV) in  $\text{Au}_{0.35}\text{Pd}_{0.5}\text{Ir}_{0.15}/\text{NH}_2\text{-N-rGO}$  are both slightly moved to the higher values [35,43–47]. Therefore, electrons in supported  $\text{Au}_{0.35}\text{Pd}_{0.5}\text{Ir}_{0.15}$  tend to transfer from Pd and Ir to Au, which is consistent with their electronegativities (Au 2.4, Pd 2.2, Ir 2.2) [35,48]. This electron iteration further proves the formation of the tri-metallic alloy of



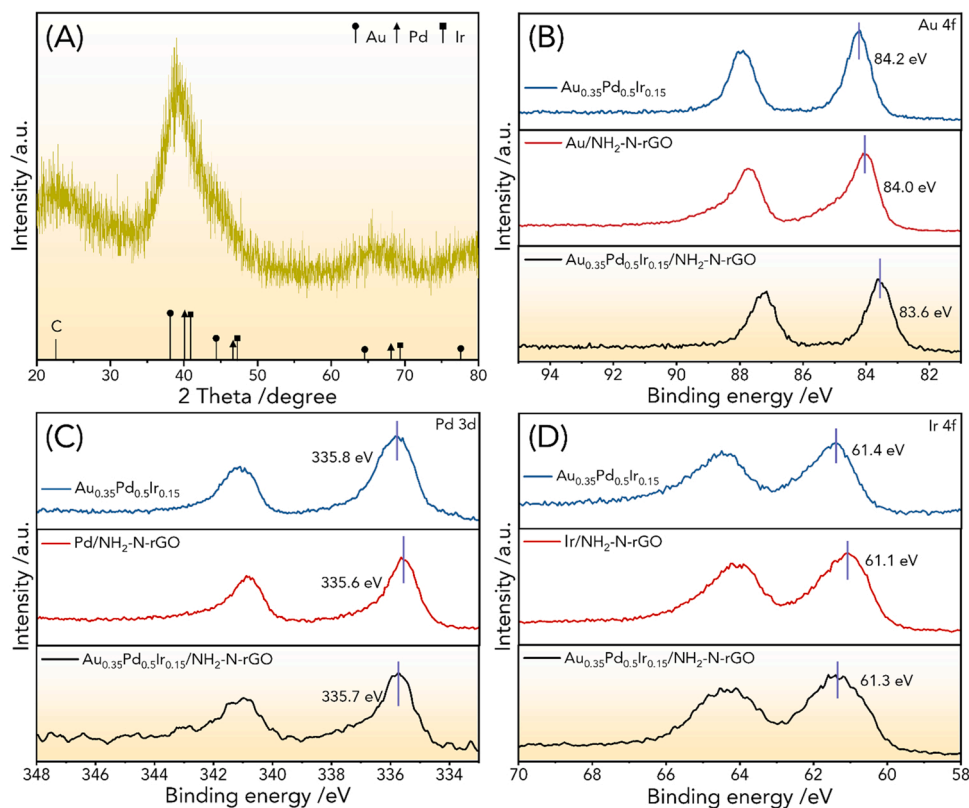


**Fig. 2.** (A) XRD pattern of  $\text{Au}_{0.35}\text{Pd}_{0.5}\text{Ir}_{0.15}/\text{NH}_2\text{-N-rGO}$ . XPS spectra of (B) Au 4f in  $\text{Au}_{0.35}\text{Pd}_{0.5}\text{Ir}_{0.15}$ ,  $\text{Au}/\text{NH}_2\text{-N-rGO}$  and  $\text{Au}_{0.35}\text{Pd}_{0.5}\text{Ir}_{0.15}/\text{NH}_2\text{-N-rGO}$ , (C) Pd 3d in  $\text{Au}_{0.35}\text{Pd}_{0.5}\text{Ir}_{0.15}$ ,  $\text{Pd}/\text{NH}_2\text{-N-rGO}$  and  $\text{Au}_{0.35}\text{Pd}_{0.5}\text{Ir}_{0.15}/\text{NH}_2\text{-N-rGO}$ , and (D) Ir 4f in  $\text{Au}_{0.35}\text{Pd}_{0.5}\text{Ir}_{0.15}$ ,  $\text{Ir}/\text{NH}_2\text{-N-rGO}$  and  $\text{Au}_{0.35}\text{Pd}_{0.5}\text{Ir}_{0.15}/\text{NH}_2\text{-N-rGO}$ .

$\text{Au}_{0.35}\text{Pd}_{0.5}\text{Ir}_{0.15}$ . Additionally, the atomic ratio of  $\text{Au}_{0.35}\text{Pd}_{0.5}\text{Ir}_{0.15}/\text{NH}_2\text{-N-rGO}$  is tested by inductively coupled plasma optical emission spectrometry (ICP-OES), and the results demonstrate that Au:

Pd: Ir in the present specimen is 35.2: 50.2: 14.6 (Table S1). Notably, after centrifuging and washing, element of B is proved to be almost non-existent in the samples by XPS, TEM-EDS, and ICP-OES (Figs. S5-6,

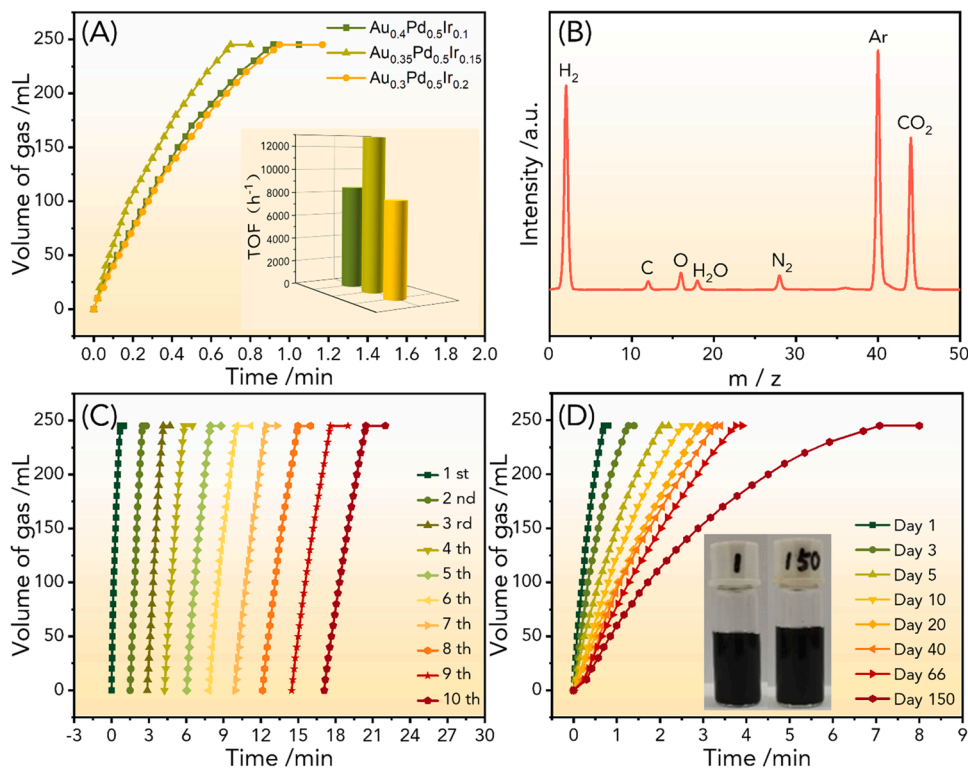


**Fig. 3.** (A) Gas generation from FA dehydrogenation (5 mmol) at 298 K versus time for  $\text{Au}_{0.4}\text{Pd}_{0.5}\text{Ir}_{0.1}$ ,  $\text{Au}_{0.35}\text{Pd}_{0.5}\text{Ir}_{0.15}$ , and  $\text{Au}_{0.3}\text{Pd}_{0.5}\text{Ir}_{0.2}$  supported on  $\text{NH}_2\text{-N-rGO}$ , with the corresponding TOF values inset. (B) MS of released gas from the dehydrogenation of FA over  $\text{Au}_{0.35}\text{Pd}_{0.5}\text{Ir}_{0.15}/\text{NH}_2\text{-N-rGO}$ . (C) Continuous recycling tests and (D) 150-day long term recycling test of  $\text{Au}_{0.35}\text{Pd}_{0.5}\text{Ir}_{0.15}/\text{NH}_2\text{-N-rGO}$  toward  $\text{H}_2$  generation from FA solution, and inset is the photo of catalysts dispersed in the reaction solution on the 1st and 150th day.

and Table S1).

Some other tri-/bi-/mono-metallic NPs supported on  $\text{NH}_2\text{-N-rGO}$  are also prepared, including  $\text{Au}_{0.4}\text{Pd}_{0.5}\text{Ir}_{0.1}$ ,  $\text{Au}_{0.3}\text{Pd}_{0.5}\text{Ir}_{0.2}$ ,  $\text{Au}_{0.5}\text{Pd}_{0.5}\text{Ir}_{0.5}$ ,  $\text{Pd}_{0.5}\text{Ir}_{0.5}$ , Au, Pd, and Ir. As we can see, the TEM images in Fig. S7 demonstrate that all the metal NPs are evenly dispersed on the substrate. And the particle sizes of  $\text{Au}_{0.4}\text{Pd}_{0.5}\text{Ir}_{0.1}$ ,  $\text{Au}_{0.3}\text{Pd}_{0.5}\text{Ir}_{0.2}$ , and  $\text{Au}_{0.5}\text{Pd}_{0.5}\text{Ir}_{0.5}$  are about 2.6, 2.7, and 2.4 nm, respectively (Fig. S8). XRD patterns show the existence of AuPdIr, AuPd, PdIr, and AuIr alloys, and the pure metallic Au, Pd, and Ir (Fig. S9). The FTIR spectra in Fig. S10 prove the same  $\text{NH}_2\text{-N-rGO}$  substrate in these tri-/bi-/mono-metallic catalysts.

### 3.2. Performance of AuPdIr catalysts

As can be seen from Fig. 3A and S11, the three tri-metallic NPs of the supported  $\text{Au}_{0.4}\text{Pd}_{0.5}\text{Ir}_{0.1}$ ,  $\text{Au}_{0.35}\text{Pd}_{0.5}\text{Ir}_{0.15}$ , and  $\text{Au}_{0.3}\text{Pd}_{0.5}\text{Ir}_{0.2}$  can complete the FA dehydrogenation (100% conversion) at room temperature within 1 min, and demonstrate the initial TOF of 8520.8, 12781.2, and 7865.3  $\text{h}^{-1}$ , respectively. This means that addition of small content of Ir to partially replace Au can really increase the activity of  $\text{Au}_{0.5}\text{Pd}_{0.5}/\text{NH}_2\text{-N-rGO}$  (initial TOF = 4445.6  $\text{h}^{-1}$ ) [35], although the catalytic activity of Ir is very poor (Fig. S11B and S11D, conversion = 1%, TOF<sub>30 min</sub> = 1.7  $\text{h}^{-1}$ ). Notably, the reaction time for the mixture of supported Au, Pd, and Ir with the same content of metal and substrate as  $\text{Au}_{0.35}\text{Pd}_{0.5}\text{Ir}_{0.15}/\text{NH}_2\text{-N-rGO}$  is up to 34.3 min (Fig. S12), which demonstrates that physical mixing of active elements can not result in superior performance, and the tri-metallic alloy structure plays an extremely important role in its high activity. Interestingly, the supported  $\text{Au}_{0.35}\text{Pd}_{0.5}\text{Ir}_{0.15}$  shows the best activity among all the present tri-/bi-/mono-metallic catalysts (Figs. 3A and S11). More interestingly, as far as we know, this supported  $\text{Au}_{0.35}\text{Pd}_{0.5}\text{Ir}_{0.15}$  catalyst is also the most excellent one relative to other heterogeneous ones for FA dehydrogenation without or even with additive (Table S2). Moreover, the initial TOF value of  $\text{Au}_{0.35}\text{Pd}_{0.5}\text{Ir}_{0.15}/\text{NH}_2\text{-N-rGO}$  can reach 36598.4  $\text{h}^{-1}$  at 333 K, which is outstanding among most of the homogeneous catalysts at the same or even higher temperature (Table S3). Mass spectrum (MS) measurement (Fig. 3B) and Gas chromatograph (GC) measurement (Fig. S13) of  $\text{Au}_{0.35}\text{Pd}_{0.5}\text{Ir}_{0.15}/\text{NH}_2\text{-N-rGO}$  show that the generated gas consists of only  $\text{H}_2$  and  $\text{CO}_2$  and no trace of CO, which confirms the 100% selectivity of  $\text{Au}_{0.35}\text{Pd}_{0.5}\text{Ir}_{0.15}/\text{NH}_2\text{-N-rGO}$  for  $\text{H}_2$  generation from FA. Additionally,  $\text{Au}_{0.35}\text{Pd}_{0.5}\text{Ir}_{0.15}$ ,  $\text{Au}_{0.35}\text{Pd}_{0.5}\text{Ir}_{0.15}\text{-APTS}$ ,  $\text{Au}_{0.35}\text{Pd}_{0.5}\text{Ir}_{0.15}/\text{rGO}$ ,  $\text{Au}_{0.35}\text{Pd}_{0.5}\text{Ir}_{0.15}/\text{N-rGO}$ ,  $\text{Au}_{0.35}\text{Pd}_{0.5}\text{Ir}_{0.15}/\text{BN}$ , and  $\text{Au}_{0.35}\text{Pd}_{0.5}\text{Ir}_{0.15}/\text{TiO}_2$  are chosen for comparison (Fig. S14). Except for  $\text{Au}_{0.35}\text{Pd}_{0.5}\text{Ir}_{0.15}\text{-APTS}$  (100% conversion, 5.47 min), pure  $\text{Au}_{0.35}\text{Pd}_{0.5}\text{Ir}_{0.15}$  and  $\text{Au}_{0.35}\text{Pd}_{0.5}\text{Ir}_{0.15}$  supported on other substrates can hardly reach 100% conversion, which may result from their bigger particle sizes, aggregations, and hydrophobicity without substrate of  $\text{NH}_2\text{-N-rGO}$  (Fig. S3 and S15). The solutions of  $\text{Au}_{0.35}\text{Pd}_{0.5}\text{Ir}_{0.15}/\text{NH}_2\text{-N-rGO}$ ,  $\text{Au}_{0.35}\text{Pd}_{0.5}\text{Ir}_{0.15}/\text{N-rGO}$ , and  $\text{Au}_{0.35}\text{Pd}_{0.5}\text{Ir}_{0.15}/\text{rGO}$  after reaction are extracted after centrifugation for ICP-OES tests. Compared with that of  $\text{Au}_{0.35}\text{Pd}_{0.5}\text{Ir}_{0.15}/\text{N-rGO}$  and  $\text{Au}_{0.35}\text{Pd}_{0.5}\text{Ir}_{0.15}/\text{rGO}$ , the mole of leaching metal of  $\text{Au}_{0.35}\text{Pd}_{0.5}\text{Ir}_{0.15}/\text{NH}_2\text{-N-rGO}$  is minimal (0.1370  $\mu\text{mol}$ , Table S4). Therefore, the hydrophilic  $\text{NH}_2\text{-N-rGO}$  substrate can improve the dispersion to enhance the activity without increasing metal leaching during reaction, which is beneficial to the long-term recycling of the catalyst.

The recycling stability of supported  $\text{Au}_{0.35}\text{Pd}_{0.5}\text{Ir}_{0.15}$  is tested through adding extra aliquot of FA solution after completion of the previous one. As shown in Fig. 3C, the supported  $\text{Au}_{0.35}\text{Pd}_{0.5}\text{Ir}_{0.15}$  also keeps the 100% conversion in each run, the corresponding reaction time and the decay of activity for  $\text{Au}_{0.35}\text{Pd}_{0.5}\text{Ir}_{0.15}/\text{NH}_2\text{-N-rGO}$  are shown in Fig. S16. The TEM image and the corresponding size distribution of the supported  $\text{Au}_{0.35}\text{Pd}_{0.5}\text{Ir}_{0.15}$  after the 10th run (Fig. S17) show that the nanoalloys are still well dispersed with a slightly increased particle size (2.8 nm). To further test the long-term stability, a 150-day experiment is designed. The catalyst after the reaction is kept under ambient, and after

several days, the aliquot of FA aqueous solution is added for recycling test. As shown in Fig. 3D, even on the 150th day, the catalyst can still lead to the 100% dehydrogenation of FA during 7.08 min at room temperature, and also shows the similar good dispersion in the reaction solution as the 1st application (Fig. 3D, inset). As a comparison, the catalytic activity of the supported  $\text{Au}_{0.5}\text{Pd}_{0.35}\text{Ir}_{0.15}$  is also tested, where part of Pd is replaced by Ir. Interestingly, the initial TOF value of  $\text{Au}_{0.5}\text{Pd}_{0.35}\text{Ir}_{0.15}/\text{NH}_2\text{-N-rGO}$  (5381.6  $\text{h}^{-1}$ ) is much lower than that of  $\text{Au}_{0.35}\text{Pd}_{0.5}\text{Ir}_{0.15}/\text{NH}_2\text{-N-rGO}$  (Fig. S18) but still higher than  $\text{Au}_{0.5}\text{Pd}_{0.5}/\text{NH}_2\text{-N-rGO}$ . Thus, it is better to replace part of Au rather than Pd with Ir to improve the performance based on the supported  $\text{Au}_{0.5}\text{Pd}_{0.5}$ .

### 3.3. DFT calculations

Based on the first-order approximation, the surface energy of AuPd and AuPdIr alloys can be calculated from arithmetic weighted average  $\gamma$  of its component metals [35]. Obviously, the calculated results show that  $\gamma$  of tri-metallic AuPdIr alloys with different molar ratios are higher than those of their corresponding bimetallic components of AuPd (Fig. S19). It is well known that the higher the  $\gamma$ , the lower the thermodynamic stability. Therefore, element Ir would not segregate on the surface of AuPdIr. In order to investigate the effect of Ir additives and simplify the calculation, we choose surface models of  $\text{Au}_{0.38}\text{Pd}_{0.5}\text{Ir}_{0.12}$  and  $\text{Au}_{0.5}\text{Pd}_{0.38}\text{Ir}_{0.12}$  to represent  $\text{Au}_{0.35}\text{Pd}_{0.5}\text{Ir}_{0.15}$  and  $\text{Au}_{0.5}\text{Pd}_{0.35}\text{Ir}_{0.15}$ , respectively. In addition, the little difference in Ir content (15 at% or 12 at%) will not lead to the differences in the morphologies and catalytic activities of the tri-metallic AuPdIr (Fig. S20).

The schematic surface model is shown in Fig. S21. The reaction pathways for  $\text{Au}_{0.38}\text{Pd}_{0.5}\text{Ir}_{0.12}$  and  $\text{Au}_{0.5}\text{Pd}_{0.38}\text{Ir}_{0.12}$  are shown in Fig. 4A. The formate ( $\text{HCOO}$ ) is considered as the intermediate of hydrogen generation from FA, and the CO formation is ignored. As a result, both  $\text{Au}_{0.38}\text{Pd}_{0.5}\text{Ir}_{0.12}$  and  $\text{Au}_{0.5}\text{Pd}_{0.38}\text{Ir}_{0.12}$  catalysts are better than  $\text{Au}_{0.5}\text{Pd}_{0.5}$ . When part of the Pd atoms is replaced by Ir atoms, TS1 is the RDS, while TS2 becomes RDS when Au atoms are replaced by Ir atoms. Obviously,  $\text{Au}_{0.38}\text{Pd}_{0.5}\text{Ir}_{0.12}$  surface has a lower RDS  $E_{\text{bar}}$  (0.53 eV) than  $\text{Au}_{0.5}\text{Pd}_{0.38}\text{Ir}_{0.12}$  (0.62 eV).

It is worth noting that the addition of Ir can change the local  $\gamma$  of the catalyst, resulting in the changes of initial adsorption configuration of  $\text{HCOOH}^*$  and  $E_{\text{bar}}$  in each reaction step. Firstly,  $\gamma$  of Ir and Pd (1.85 J/ $\text{m}^2$ ) are higher than Au [36]. Therefore, sites of Ir and Pd on the surface of AuPdIr have stronger adsorption abilities than that of Au [35]. This results in the formation of O-Ir and O-Pd bonds of  $\text{HCOOH}^*$  on  $\text{Au}_{0.38}\text{Pd}_{0.5}\text{Ir}_{0.12}$  but not two O-Pd bonds on  $\text{Au}_{0.5}\text{Pd}_{0.5}$  (Fig. 4B). The O-H bond lengths on  $\text{Au}_{0.5}\text{Pd}_{0.5}$  and  $\text{Au}_{0.38}\text{Pd}_{0.5}\text{Ir}_{0.12}$  are calculated to be 1.005 Å and 1.016 Å, respectively. The longer O-H bond on  $\text{Au}_{0.38}\text{Pd}_{0.5}\text{Ir}_{0.12}$  is easier to be broken, implying a lower  $E_{\text{bar}}$ (TS1) than that on  $\text{Au}_{0.5}\text{Pd}_{0.5}$  surface. The optimized geometry configurations and the electron redistribution of the formed bi- $\text{HCOO}^*$  on  $\text{Au}_{0.5}\text{Pd}_{0.5}$  and  $\text{Au}_{0.38}\text{Pd}_{0.5}\text{Ir}_{0.12}$  are shown in Fig. 4C. Interestingly, the symmetric in adsorption configuration of bi- $\text{HCOO}^*$  on  $\text{Au}_{0.38}\text{Pd}_{0.5}\text{Ir}_{0.12}$  is different from  $\text{Au}_{0.5}\text{Pd}_{0.5}$ . Compared with  $\text{Au}_{0.5}\text{Pd}_{0.5}$ , there is an area with a slightly faded color in the charge density difference plots (maximum of 0.11  $\text{e}/\text{\AA}^3$ ) of  $\text{Au}_{0.38}\text{Pd}_{0.5}\text{Ir}_{0.12}$ , and more electrons accumulate between O and Ir atoms, demonstrating a stronger charge transfer from O to Ir atom (maximum of 0.17  $\text{e}/\text{\AA}^3$ ). The elongation of bond length (from 2.21 Å to 2.26 Å) and reduction of vibration frequency (from 258.2  $\text{cm}^{-1}$  to 239.0  $\text{cm}^{-1}$ ) of O-Pd bond are observed on  $\text{Au}_{0.38}\text{Pd}_{0.5}\text{Ir}_{0.12}$ . Thus, the weaker O-Pd bond belonging to  $\text{Au}_{0.38}\text{Pd}_{0.5}\text{Ir}_{0.12}$  results in a lower RDS  $E_{\text{bar}}$ (TS2) on  $\text{Au}_{0.38}\text{Pd}_{0.5}\text{Ir}_{0.12}$  than that on  $\text{Au}_{0.5}\text{Pd}_{0.5}$ .

Based on the above calculation, it is certain that the addition of Ir into AuPd can change the initial adsorption configuration of  $\text{HCOOH}^*$  and break the symmetry of bi- $\text{HCOO}^*$  adsorption configuration. Therefore, the  $E_{\text{bar}}$ (TS1) and  $E_{\text{bar}}$ (TS2) decrease simultaneously, which endows the better catalytic activity of  $\text{Au}_{0.38}\text{Pd}_{0.5}\text{Ir}_{0.12}$  than  $\text{Au}_{0.5}\text{Pd}_{0.5}$ .

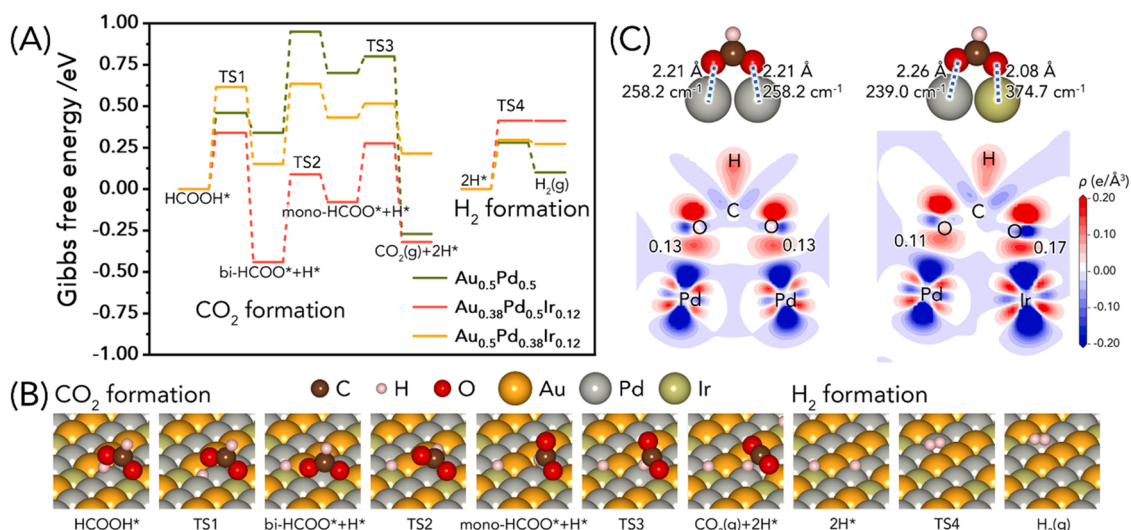


**Fig. 4.** DFT calculations for the dehydrogenation from formic acid on AuPdIr surface. (A) The reaction pathway of FA dehydrogenation is calculated via H-COO pathway on  $\text{Au}_{0.5}\text{Pd}_{0.5}$  [35],  $\text{Au}_{0.38}\text{Pd}_{0.5}\text{Ir}_{0.12}$ , and  $\text{Au}_{0.5}\text{Pd}_{0.38}\text{Ir}_{0.12}$ . (B) The configuration and transition state of each step on  $\text{Au}_{0.38}\text{Pd}_{0.5}\text{Ir}_{0.12}$  surface, the gray, yellow, green, brown, red, and pink atoms indicate the Pd, Au, Ir, C, O, and H, respectively. (C) The optimized geometry configurations and the electron redistribution with the difference of electron density of bi-HCOO\* on  $\text{Au}_{0.5}\text{Pd}_{0.5}$  and  $\text{Au}_{0.38}\text{Pd}_{0.5}\text{Ir}_{0.12}$  surface in step two (TS2).

### 3.4. Characterization and performances of other tri-metallic catalysts

By DFT calculation, it is proved that the excellent performance of AuPdIr NPs is attributed to the high  $\gamma$  of Ir. In order to further verify that adding a high  $\gamma$  element to replace some of Au atoms can truly improve the performance of  $\text{Au}_{0.5}\text{Pd}_{0.5}/\text{NH}_2\text{-N-rGO}$ , other supported AuPdM (M=Pt, Rh, and Ru) systems are prepared. Notably, the  $\gamma$  of Pt, Rh, and Ru are 2.54, 2.7, and 3.93 J/m<sup>2</sup>, respectively [36].

The TEM images in Fig. 5A-B demonstrate that  $\text{Au}_{0.44}\text{Pd}_{0.5}\text{Pt}_{0.06}$  NPs

are distinctly anchored on  $\text{NH}_2\text{-N-rGO}$  substrate, and the mean particle size is the same as  $\text{Au}_{0.35}\text{Pd}_{0.5}\text{Ir}_{0.15}$  NPs (2.6 nm). XRD pattern (Fig. 5C) demonstrates the formation of  $\text{Au}_{0.44}\text{Pd}_{0.5}\text{Pt}_{0.06}$  nanoalloy due to the peak of (111) plane is between those of fcc Au (JCPDS: 65-2870), Pd (JCPDS: 65-2867), and Pt (JCPDS: 65-2868) [35].

Fig. 5D shows the catalytic activity of the supported  $\text{Au}_{0.44}\text{Pd}_{0.5}\text{Pt}_{0.06}$ . It can be seen that  $\text{Au}_{0.44}\text{Pd}_{0.5}\text{Pt}_{0.06}/\text{NH}_2\text{-N-rGO}$  also has a good performance with initial TOF of 10224.9 h<sup>-1</sup> and 100% conversion within 0.73 min. This TOF value is much better than that of

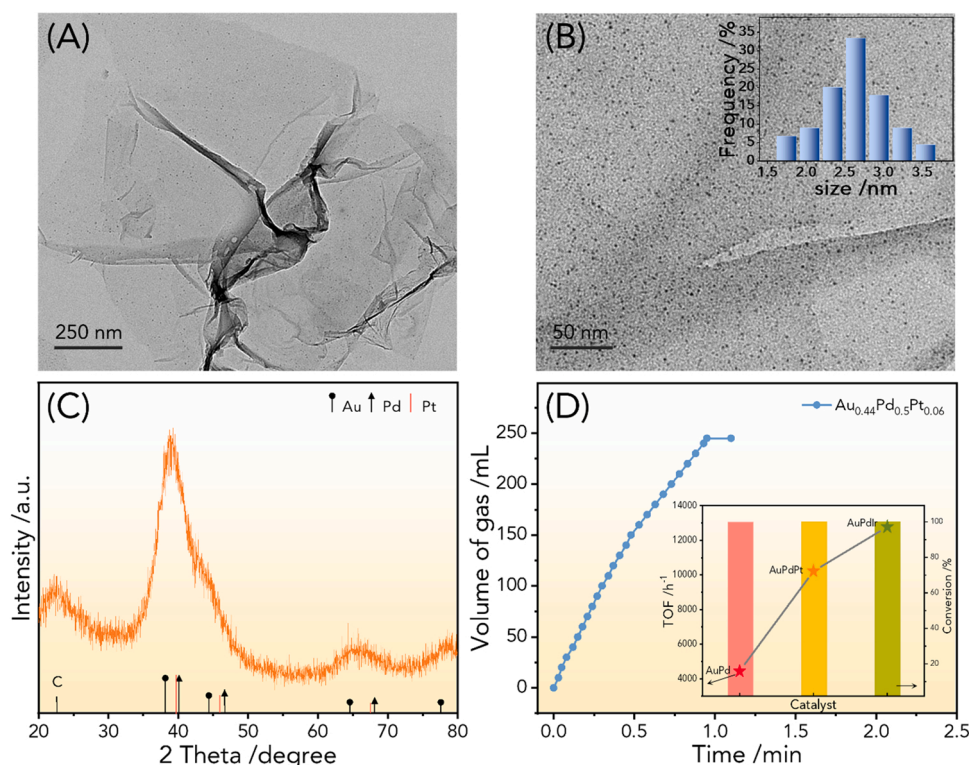


**Fig. 5.** TEM images of  $\text{Au}_{0.44}\text{Pd}_{0.5}\text{Pt}_{0.06}/\text{NH}_2\text{-N-rGO}$  with (A) low and (B) middle resolutions, and inset is the corresponding size distribution. (C) XRD pattern of  $\text{Au}_{0.44}\text{Pd}_{0.5}\text{Pt}_{0.06}/\text{NH}_2\text{-N-rGO}$ . (D) Gas generation from FA dehydrogenation (5 mmol) at 298 K versus time for  $\text{Au}_{0.44}\text{Pd}_{0.5}\text{Pt}_{0.06}/\text{NH}_2\text{-N-rGO}$ , and inset is the TOF values and conversion of  $\text{Au}_{0.35}\text{Pd}_{0.5}\text{Ir}_{0.15}$ ,  $\text{Au}_{0.44}\text{Pd}_{0.5}\text{Pt}_{0.06}$ , and  $\text{Au}_{0.5}\text{Pd}_{0.5}$  supported on  $\text{NH}_2\text{-N-rGO}$ .



Au<sub>0.5</sub>Pd<sub>0.5</sub>/NH<sub>2</sub>-N-rGO and comparable to that of Au<sub>0.35</sub>Pd<sub>0.5</sub>Ir<sub>0.15</sub>/NH<sub>2</sub>-N-rGO (Fig. 5D, inset). The atomic ratio of Au: Pd: Pt in the present specimen is tested to be 44.2: 50.1: 5.7 by ICP-OES (Table S5). MS measurement shows that the generated gas consists of only H<sub>2</sub> and CO<sub>2</sub> and no trace of CO (Fig. S22), which confirms that the 100% selectivity of the supported Au<sub>0.44</sub>Pd<sub>0.5</sub>Pt<sub>0.06</sub> for H<sub>2</sub> generation from FA. It should be noted that more or less atomic ratio of Pt in AuPdPt system results in the decrease of its activity (Fig. S23) even with similar particle sizes and dispersions (Fig. S24).

Additionally, the reaction time of Au<sub>0.42</sub>Pd<sub>0.5</sub>Rh<sub>0.08</sub>/NH<sub>2</sub>-N-rGO and Au<sub>0.44</sub>Pd<sub>0.5</sub>Ru<sub>0.06</sub>/NH<sub>2</sub>-N-rGO are 1.47 and 1.3 min (Figs. S25 and S26), respectively, which are both shorter than that of Au<sub>0.5</sub>Pd<sub>0.5</sub>/NH<sub>2</sub>-N-rGO. The corresponding TEM images and XRD patterns are shown in Fig. S27–30. Notably, the supported AuPdRu system is worse than the AuPdIr system, which may be because too high  $\gamma$  is disadvantageous to HCOO\* desorption.

On the basis of above results, it can be reasonably proposed that the partial replacement of Au by an element with relatively high  $\gamma$  is a novel way to improve the activity of bimetallic AuPd catalyst toward hydrogen generation from FA.

#### 4. Conclusion

In summary, alloying of AuPd with an element which has a higher  $\gamma$  than Pd, such as Ir, Pt, Rh, or Ru is a feasible way to increase the catalytic activity toward FA dehydrogenation. In particular, Au<sub>0.35</sub>Pd<sub>0.5</sub>Ir<sub>0.15</sub> nanoalloys with the initial TOF value of 12781.2 h<sup>-1</sup> is durable, and displays 100% selectivity of H<sub>2</sub> and 100% conversion even after 150 days, which is never reached by other heterogeneous catalysts. Based on the DFT calculation, this robust activity is attributed to the addition of high  $\gamma$  element of Ir, leading to the change of the initial adsorption configuration of HCOOH\*, which breaks the symmetry of bi-HCOO\* adsorption configurations to reduce the  $E_{\text{bar}}$ (TS1) and  $E_{\text{bar}}$ (TS2) simultaneously. This new strategy to improve the activity of the bimetallic AuPd catalyst is also proved by addition of other elements of high  $\gamma$  (Pt, Rh, and Ru). The easy and rapid synthesis methods and the excellent performances of the present tri-metallic catalysts may promote the further commercial application of FA as a hydrogen storage/generation material.

#### CRediT authorship contribution statement

**Dong-Xue Liu:** Conceptualization, Investigation, Writing-original draft. **Yi-Tong Zhou:** Software, Writing – original draft. **Yong-Fu Zhu:** Writing – review & editing. **Ze-Yu Chen:** Writing – review & editing. **Jun-Min Yan:** Conceptualization, Supervision, Writing – review & editing. **Qing Jiang:** Writing – review & editing.

#### Declaration of Competing Interest

The authors declare that they have no known competing financial interests or personal relationships that could have appeared to influence the work reported in this paper.

#### Acknowledgments

This work is supported in part by National Natural Science Foundation of China (51925102); National Key R & D Program of China (2020YFB1505603). We sincerely appreciate Prof. Wei Liu at Nanjing University of Science & Technology for his valuable discussion on DFT calculation.

#### Appendix A. Supporting information

Supplementary data associated with this article can be found in the online version at doi:10.1016/j.apcatb.2022.121228.

#### References

- [1] Q.Y. Bi, J.D. Lin, Y.M. Liu, H.Y. He, F.Q. Huang, Y. Cao, Dehydrogenation of formic acid at room temperature: boosting Palladium nanoparticle efficiency by coupling with pyridine-nitrogen-doped carbon, *Angew. Chem. Int. Ed.* 55 (2016) 11849–11853, <https://doi.org/10.1002/anie.201605961>.
- [2] L. Schlapbach, A. Züttel, Hydrogen-storage materials for mobile applications, *Nature* 414 (2001) 353–358, <https://doi.org/10.1038/35104634>.
- [3] Z.L. Wang, X.F. Hao, Z. Jiang, X.P. Sun, D. Xu, J. Wang, H.X. Zhong, F.L. Meng, X. B. Zhang, C and N hybrid coordination derived Co-C-N complex as a highly efficient electrocatalyst for hydrogen evolution reaction, *J. Am. Chem. Soc.* 137 (2015) 15070–15073, <https://doi.org/10.1021/jacs.5b09021>.
- [4] A. Ahadi, H. Alamgholiloo, S. Rostamnia, X. Liu, M. Shokouhimehr, D.A. Alonso, R. Luque, Layer-wise titania growth within dimeric organic functional group viologen periodic mesoporous organosilica as efficient photocatalyst for oxidative, *ChemCatChem* 11 (2019) 4803–4809, <https://doi.org/10.1002/cctc.201900486>.
- [5] Q.L. Zhu, Q. Xu, Liquid organic and inorganic chemical hydrides for high-capacity hydrogen storage, *Energy Environ. Sci.* 8 (2015) 478–512, <https://doi.org/10.1039/c4ee03690e>.
- [6] T.C. Johnson, D.J. Morris, M. Wills, Hydrogen generation from formic acid and alcohols using homogeneous catalysts, *Chem. Soc. Rev.* 39 (2010) 81–88, <https://doi.org/10.1039/b904495g>.
- [7] F. Joo, Breakthroughs in hydrogen storage–formic acid as a sustainable storage material for hydrogen, *ChemSusChem* 1 (2008) 805–808, <https://doi.org/10.1002/cssc.200800133>.
- [8] H. Zhong, M. Iguchi, M. Chatterjee, Y. Himeda, Q. Xu, H. Kawanami, Formic acid-based liquid organic hydrogen carrier system with heterogeneous catalysts, *Adv. Sustain. Syst.* 2 (2018), 1700161, <https://doi.org/10.1002/adsu.201700161>.
- [9] C. Feng, S.T. Gao, N.Z. Shang, X. Zhou, C. Wang, Super nanotetragonal ZrO<sub>2</sub> embedded in carbon as efficient support of PdAg nanoparticle for boosting hydrogen generation from formic acid, *Energy Technol.* 6 (2018) 2120–2125, <https://doi.org/10.1002/ente.201800319>.
- [10] H.L. Jiang, S.K. Singh, J.M. Yan, X.B. Zhang, Q. Xu, Liquid-phase chemical hydrogen storage: catalytic hydrogen generation under ambient conditions, *ChemSusChem* 3 (2010) 541–549, <https://doi.org/10.1002/cssc.201000023>.
- [11] A. Léval, H. Junge, M. Beller, Formic acid dehydrogenation by a cyclometalated  $\kappa^3$ -CNN Ruthenium complex, *Eur. J. Inorg. Chem.* 14 (2020) 1293–1299, <https://doi.org/10.1002/ejic.202000068>.
- [12] C. Guan, Y.P. Pan, T.H. Zhang, M.J. Ajitha, K.W. Huang, An update on formic acid dehydrogenation by homogeneous catalysis, *Chem. Asian J.* 15 (2020) 937–946, <https://doi.org/10.1002/asia.201901676>.
- [13] C. Fink, G. Laurenczy, A precious catalyst: Rhodium-catalyzed formic acid dehydrogenation in water, *Eur. J. Inorg. Chem.* 18 (2019) 2381–2387, <https://doi.org/10.1002/ejic.201900344>.
- [14] A. Agapova, E. Alberico, A. Kammer, H. Junge, M. Beller, Catalytic dehydrogenation of formic acid with Ruthenium-PNP-pincer complexes: comparing N-methylated and NH-ligands, *ChemCatChem* 11 (2019) 1910–1914, <https://doi.org/10.1002/cctc.201801897>.
- [15] L. Wang, N. Onishi, K. Murata, T. Hirose, J.T. Muckerman, E. Fujita, Y. Himeda, Efficient hydrogen storage and production using a catalyst with an imidazoline-based, proton-responsive ligand, *ChemSusChem* 10 (2017) 1071–1075, <https://doi.org/10.1002/cssc.201601437>.
- [16] Z.J. Wang, S.M. Lu, J. Li, J.J. Wang, C. Li, Unprecedentedly high formic acid dehydrogenation activity on an iridium complex with an N, N'-diimine ligand in water, *Chem. Eur. J.* 21 (2015) 12592–12595, <https://doi.org/10.1002/chem.201502086>.
- [17] J.B. Curley, W.H. Bernskoetter, N. Hazari, Additive-free formic acid dehydrogenation using a pincer-supported iron catalyst, *ChemCatChem* 12 (2020) 1934–1938, <https://doi.org/10.1002/cctc.202000066>.
- [18] R.M. Irfan, T.T. Wang, D.C. Jiang, Q.D. Yue, L. Zhang, H.Y. Cao, Y. Pan, P.W. Du, Homogeneous molecular iron catalysts for direct photocatalytic conversion of formic acid to syngas (CO+H<sub>2</sub>), *Angew. Chem. Int. Ed.* 59 (2020) 14818–14824, <https://doi.org/10.1002/anie.202002757>.
- [19] S. Jones, J. Qu, K. Tedsree, X.Q. Gong, S.C. Tsang, Prominent electronic and geometric modifications of palladium nanoparticles by polymer stabilizers for hydrogen production under ambient conditions, *Angew. Chem. Int. Ed.* 51 (2012) 11275–11278, <https://doi.org/10.1002/anie.201206035>.
- [20] Y.Y. Cai, X.H. Li, Y.N. Zhang, X. Wei, K.X. Wang, J.S. Chen, Highly efficient dehydrogenation of formic acid over a palladium-nanoparticle-based Mott-Schottky photocatalyst, *Angew. Chem. Int. Ed.* 52 (2013) 11822–11825, <https://doi.org/10.1002/anie.201304652>.
- [21] O.Y. Podyacheva, D.A. Bulushev, A.N. Suboch, D.A. Svintitskiy, A.S. Lisitsyn, E. Modin, A. Chuvilin, E.-Y. Gerasimov, V.-I. Sobolev, V.-N. Parmon, Highly stable single-atom catalyst with ionic Pd active sites supported on N-Doped carbon nanotubes for formic acid decomposition, *ChemSusChem* 11 (2018) 3724–3727, <https://doi.org/10.1002/cssc.201801679>.
- [22] H. Alamgholiloo, S. Rostamnia, A. Hassankhani, X. Liu, A. Eftekhari, A. Hasanzadeh, K. Zhang, H.K. Maleh, S. Khaksar, R.S. Varma, M. Shokouhimehr, Formation and stabilization of colloidal ultra-small palladium nanoparticles on diamine-modified Cr-MIL-101: synergic boost to hydrogen production from formic acid, *J. Colloid Interf. Sci.* 567 (2020) 126–135, <https://doi.org/10.1016/j.jcis.2020.01.087>.
- [23] N. Nouruzi, M. Dinari, N. Mokhtari, M. Farajzadeh, B. Gholipour, S. Rostamnia, Selective catalytic generation of hydrogen over covalent organic polymer supported Pd nanoparticles (COP-Pd), *Mol. Catal.* 493 (2020), 111057, <https://doi.org/10.1016/j.mcat.2020.111057>.

- [24] M. Farajzadeh, H. Alamgholiloo, F. Nasibipour, R. Banaei, S. Rostamnia, Anchoring Pd-nanoparticles on dithiocarbamate-functionalized SBA-15 for hydrogen generation from formic acid, *Sci. Rep.* 10 (2020) 18188, <https://doi.org/10.1038/s41598-020-75369-y>.
- [25] E. Doustkhah, H. Mohtasham, M. Farajzadeh, S. Rostamnia, Y. Wang, H. Arandian, M.H.N. Assadi, Organosiloxane tunability in mesoporous organosilica and punctuated Pd nanoparticles growth; theory and experiment, *Micro Mesopor. Mat.* 293 (2020), 109832, <https://doi.org/10.1016/j.micromeso.2019.109832>.
- [26] N. Nouruzi, M. Dinari, B. Gholipour, N. Mokhtari, M. Farajzadeh, S. Rostamnia, M. Shokouhimehr, Photocatalytic hydrogen generation using colloidal covalent organic polymers decorated bimetallic Au-Pd nanoalloy (COPs/Pd-Au), *Mol. Catal.* 518 (2022), 112058, <https://doi.org/10.1016/j.mcat.2021.112058>.
- [27] E. Doustkhah, M. Hasani, Y. Ide, M.N. Assadi, Pd nanoalloys for H<sub>2</sub> generation from formic acid, *ACS Appl. Nano Mater.* 3 (2020) 22–43, <https://doi.org/10.1021/acsnm.9b02004>.
- [28] J.M. Yan, S.J. Li, S.S. Yi, B.R. Wulan, W.T. Zheng, Q. Jiang, Anchoring and upgrading ultrafine NiPd on room-temperature-synthesized bifunctional NH<sub>2</sub>-N-rGO toward low-cost and highly efficient catalysts for selective formic acid dehydrogenation, *Adv. Mater.* 30 (2018), 1703038, <https://doi.org/10.1002/adma.201703038>.
- [29] L. Yang, X. Hua, J. Su, W. Luo, S.L. Chen, G.Z. Cheng, Highly efficient hydrogen generation from formic acid-sodium formate over monodisperse AgPd nanoparticles at room temperature, *Appl. Catal. B: Environ.* 168–169 (2015) 423–428, <https://doi.org/10.1016/j.apcatb.2015.01.003>.
- [30] Z.L. Wang, J.M. Yan, Y.F. Zhang, Y. Ping, H.L. Wang, Q. Jiang, Facile synthesis of nitrogen-doped graphene supported AuPd-CeO<sub>2</sub> nanocomposites with high-performance for hydrogen generation from formic acid at room temperature, *Nanoscale* 6 (2014) 3073–3077, <https://doi.org/10.1039/c3nr05809c>.
- [31] J.M. Yan, Z.L. Wang, L. Gu, S.J. Li, H.L. Wang, W.T. Zheng, Q. Jiang, AuPd-MnO<sub>x</sub>/MOF-graphene: an efficient catalyst for hydrogen production from formic acid at room temperature, *Adv. Energy Mater.* 5 (2015), 1500107, <https://doi.org/10.1002/aenm.201500107>.
- [32] X.C. Yang, P. Pachfule, Y. Chen, N. Tsumori, Q. Xu, Highly efficient hydrogen generation from formic acid using a reduced graphene oxide-supported AuPd nanoparticle catalyst, *Chem. Commun.* 52 (2016) 4171–4174, <https://doi.org/10.1039/c5cc10311h>.
- [33] S. Wu, F. Yang, H. Wang, R. Chen, P.C. Sun, T.H. Chen, Mg<sup>2+</sup>-assisted low temperature reduction of alloyed AuPd/C: an efficient catalyst for hydrogen generation from formic acid at room temperature, *Chem. Commun.* 51 (2015) 10887–10890, <https://doi.org/10.1039/c5cc02604k>.
- [34] S. Wu, F. Yang, P.C. Sun, T.H. Chen, Au-Pd alloy catalyst with high performance for hydrogen generation from formic acid-formate solution at nearly 0 °C, *RSC Adv.* 4 (2014) 44500–44503, <https://doi.org/10.1039/c4ra08389j>.
- [35] S.J. Li, Y.T. Zhou, X. Kang, D.X. Liu, L. Gu, Q.H. Zhang, J.M. Yan, Q. Jiang, A simple and effective principle for a rational design of heterogeneous catalysts for dehydrogenation of formic acid, *Adv. Mater.* 31 (2019), 1806781, <https://doi.org/10.1002/adma.201806781>.
- [36] Q. Jiang, H.M. Lu, M. Zhao, Modelling of surface energies of elemental crystals, *J. Phys.: Condens. Matter* 16 (2004) 521–530, <https://doi.org/10.1088/0953-8984/16/4/001>.
- [37] A. Vasileff, Y. Zheng, S.Z. Qiao, Carbon solving carbon's problems: recent progress of nanostructured carbon-based catalysts for the electrochemical reduction of CO<sub>2</sub>, *Adv. Energy Mater.* 7 (2017), 1700759, <https://doi.org/10.1002/aenm.201700759>.
- [38] A.K. Singh, S. Jang, J.Y. Kim, S. Sharma, K.C. Basavaraju, M.G. Kim, K.R. Kim, J. S. Lee, H.H. Lee, D.P. Kim, One-pot defunctionalization of lignin-derived compounds by dual-functional Pd<sub>50</sub>Ag<sub>50</sub>/Fe<sub>3</sub>O<sub>4</sub>/N-rGO catalyst, *ACS Catal.* 5 (2015) 6964–6972, <https://doi.org/10.1021/acscatal.5b01319>.
- [39] C. Xia, Y. Qiu, Y. Xia, P. Zhu, G. King, X. Zhang, Z. Wu, J.Y. Kim, D.A. Cullen, D. Zheng, P. Li, M. Shakouri, E. Heredia, P. Cui, H.N. Alshareef, Y. Hu, H. Wang, General synthesis of single-atom catalysts with high metal loading using graphene quantum dots, *Nat. Chem.* 13 (2021) 887–894, <https://doi.org/10.1038/s41557-021-00734-x>.
- [40] S.J. Li, Y. Ping, J.M. Yan, H.L. Wang, M. Wu, Q. Jiang, Facile synthesis of AgAuPd/graphene with high performance for hydrogen generation from formic acid, *J. Mater. Chem. A* 3 (2015) 14535–14538, <https://doi.org/10.1039/c5ta03111g>.
- [41] J. Roller, J.A. Jimenez, R. Jain, H. Yu, R. Maric, C.B. Carter, Processing, Activity and microstructure of oxygen evolution anodes prepared by a dry and direct deposition technique, *ECS Trans.* 45 (2013) 97–106, <https://doi.org/10.1149/04521.009ecst>.
- [42] M.A. Isaacs, C.M.A. Parlett, N. Robinson, L.J. Durnell, J.C. Manayil, S. K. Beaumont, S. Jiang, N.S. Hondow, A.C. Lamb, D. Jampaiah, M.L. Johns, K. Wilson, A.F. Lee, A spatially orthogonal hierarchically porous acid–base catalyst for cascade and antagonistic reactions, *Nat. Catal.* 3 (2020) 921–931, <https://doi.org/10.1038/s41929-020-00526-5>.
- [43] L.M. Wu, B.X. Ni, R. Chen, C.X. Shi, P.C. Sun, T.H. Chen, Ultrafine PdAu nanoparticles immobilized on amine functionalized carbon black toward fast dehydrogenation of formic acid at room temperature, *Nanoscale Adv.* 1 (2019) 4415–4421, <https://doi.org/10.1039/c9na00462a>.
- [44] J. Beran, K. Masek, RHEED and XPS study of palladium interaction with cerium oxide surface, *Vacuum* 167 (2019) 438–444, <https://doi.org/10.1016/j.vacuum.2019.06.023>.
- [45] K.C. Lee, O. Savadogo, A. Ishihara, S. Mitsushima, N. Kamiya, K. Ota, Methanol-tolerant oxygen reduction electrocatalysts based on Pd-3D transition metal alloys for direct methanol fuel cells, *J. Electrochem. Soc.* 153 (2006) A20–A24, <https://doi.org/10.1149/1.2128101>.
- [46] E.N.E. Sawy, V.I. Birss, Nano-porous iridium and iridium oxide thin films formed by high efficiency electrodeposition, *J. Mater. Chem.* 1 (2009) 8244–8252, <https://doi.org/10.1039/b914662h>.
- [47] B. Jiang, Y.N. Guo, J. Kim, A.E. Whitten, K. Wood, K. Kani, A.E. Rowan, J. Henzie, Y. Yamauchi, Mesoporous metallic iridium nanosheets, *J. Am. Chem. Soc.* 140 (2018) 12434–12441, <https://doi.org/10.1021/jacs.8b05206>.
- [48] W. Sun, L.M. Cao, J. Yang, Conversion of inert cryptomelane-type manganese oxide into a highly efficient oxygen evolution catalyst via limited Ir doping, *J. Mater. Chem. A* 4 (2016) 12561–12570, <https://doi.org/10.1039/c6ta03011d>.